Research Article | Vol. 25, No. 10 | 15 May 2017 | OPTICS EXPRESS 11009

Optics EXPRESS

Analog signal processing in the terahertz communication links using waveguide Bragg gratings: example of dispersion compensation

Tian Ma, Kathirvel Nallapan, Hichem Guerboukha and Maksim Skorobogatiy*

Department of Engineering Physics, École Polytechnique de Montréal, Montreal, Québec, H3T 1J4, Canada

*maksim.skorobogatiy@polymtl.ca

Abstract: We study the possibility of analog signal processing for the upcoming terahertz (THz) high-bitrate communications using as an example the problem of dispersion compensation in the THz communication links. In particular, two Waveguide Bragg Grating devices (WBGs) operating in the transmission mode are detailed. WBGs are designed by introducing periodic corrugation onto the inner surface of the metalized tubes. The resultant devices operate in a single mode regime either in the vicinity of the modal cutoff or in the vicinity of a bandgap edge, featuring large negative group velocity dispersions (GVD). We fabricate the proposed WBGs using 3D stereolithography, and metallize them using wet chemistry. Optical properties of the fabricated WBGs are investigated both theoretically and experimentally. The results confirm single mode guidance, relatively high coupling efficiency, as well as large negative group velocity dispersions in the range of several $-100's$ $\mathrm{ps}/(\mathrm{THz}\cdot\mathrm{cm})$ in the vicinity of 0.14THz. This makes the short sections of proposed WBGs suitable for compensating positive dispersion incurred in the THz wireless links or fiber-assisted THz interconnects for signals of several-GHz bandwidth. Finally, we comment on the challenges associated with the analog signal processing in the THz spectral range.

OCIS codes: (040.2235) Far infrared or terahertz; (060.2310) Fiber optic; (060.3735) Fiber Bragg gratings; (350.4238) Nanophotonics and photonic crystals.

References and Links

1. I. F. Akyildiz, J. M. Jornet, and C. Han, "Terahertz band: Next frontier for wireless communications," Phys. Commun. J. **12**, 16–32 (2014).
2. T. Nagatsuma, S. Horiguchi, Y. Minamikata, Y. Yoshimizu, S. Hisatake, S. Kuwano, N. Yoshimoto, J. Terada, and H. Takahashi, "Terahertz wireless communications based on photonics technologies," Opt. Express **21**, 23736-23747 (2013).
3. S. Koenig, D. Lopez-Diaz, J. Antes1, F. Boes1, R. Henneberger, A. Leuther, A. Tessmann, R. Schmogrow, D. Hillerkuss, R. Palmer, T. Zwick, C. Koos, W. Freude, O. Ambacher, J. Leuthold, and I. Kallfass, "Wireless sub-THz communication system with high data rate," Nature Photon. **7**, 977-981 (2013).
4. T. Nagatsuma, G. Ducournau, and C. C. Renaud, "Advances in terahertz communications accelerated by photonics," Nature Photon. **10**, 371-379 (2016).
5. L. J. Chen, H. W. Chen, T. F. Kao, J. Y. Lu, and C. K. Sun, "Low-loss subwavelength plastic fiber for terahertz waveguiding," Opt. Lett. **31**, 308-310 (2006).
6. A. Hassani, A. Dupuis, and M. Skorobogatiy, "Low loss porous terahertz fibers containing multiple subwavelength holes", Appl. Phys. Lett. **92**, 071101-1-071101-3 (2008).
7. A. Hassani, A. Dupuis, and M. Skorobogatiy, "Porous polymer fibers for low-loss Terahertz guiding," Opt. Express **16**, 6340-6351 (2008).
8. T. Ma, A. Markov, L. Wang, M. Skorobogatiy, "Graded index porous optical fibers – dispersion management in terahertz range," Opt. Express **23**, 7856-7869 (2015).
9. L. Vincetti, "Hollow core photonic band gap fiber for THz applications," Microw. Opt. Technol. Lett. **51**, 1711–1714, (2009).
10. K. Nielsen, H. K. Rasmussen, P. U. Jepsen, and O. Bang, "Porous-core honeycomb bandgap THz fiber," Opt. Lett. **36**, 666–668 (2011).
11. M. Skorobogatiy and A. Dupuis, "Ferroelectric all-polymer hollow Bragg fibers for terahertz guidance," Appl. Phys. Lett. **90**, 113514 (2007).

#286951 https://doi.org/10.1364/OE.25.011009
Journal © 2018 Received 16 Feb 2017; revised 20 Apr 2017; accepted 28 Apr 2017; published 3 May 2017

Optics EXPRESS

12. A. Dupuis, K. Stoeffler, B. Ung, C. Dubois, and M. Skorobogatiy, "Transmission measurements of hollow-core THz Bragg fibers," J. Opt. Soc. Am. B **28**, 896-907 (2011).
13. T. Ma, H. Guerboukha, M. Girard, A.D. Squires, R.A. Lewis, and M. Skorobogatiy "3D Printed Hollow-Core Terahertz Optical Waveguides with Hyperuniform Disordered Dielectric Reflectors," Adv. Opt. Mater. **4**, 2085-2094 (2016).
14. C. H. Lai, Y. Hsueh, H. Chen, Y. Huang, H. Chang, and C. Sun, "Low-index terahertz pipe waveguides," Opt. Lett. **34**, 3457-3459 (2009).
15. Y. Y. Wang, N. V. Wheeler, F. Couny, P. J. Roberts, and F. Benabid, "Low loss broadband transmission in hypocycloid-core Kagome hollow-core photonic crystal fiber," Opt. Lett. **36**, 669–671 (2011).
16. G. P. Agrawal, *Lightwave technology: Telecommunication systems*, (Wiley, 2005).
17. Y. Yang, M. Mandehgar, and D. Grischkowsky, "Understanding THz pulse transmission in the atmosphere," IEEE Trans. THz Sci. Technol. **2**, 406–415 (2012).
18. K. Wang and D. M. Mittleman, "Metal wires for terahertz wave guiding," Nature **432**, 376-379 (2004).
19. S. Ramachandran, *Fiber based dispersion compensation* (Springer, 2007).
20. T. Fobbe, S. Markmann, F. Fobbe, N. Hekmat, H. Nong, S. Pal, P. Balzerwoski, J. Savolainen, M. Havenith, A. D. Wieck, and N. Jukam, "Broadband terahertz dispersion control in hybrid waveguides," Opt. Express **24**, 22319-22333 (2016).
21. Z. Gao, F. Gao, K. K. Shastri, and B. Zhang, "Frequency-selective propagation of localized spoof surface plasmons in a graded plasmonic resonator chain," Sci. Rep. **6**, 25576 (2016).
22. K. O. Hill, F. Bilodeau, B. Malo, T. Kitagawa, S. Thériault, D. C. Johnson, J. Albert, and K. Takiguchi, "Chirped in-fiber Bragg gratings for compensation of optical-fiber dispersion," Opt. Lett. **19**, 1314-1316 (1994).
23. Z. Li, H. Chi, X. Zhang, and J. P. Yao, "Optical single-sideband modulation using a fiber-Bragg-grating-based optical Hilbert transformer," IEEE Photon. Technol. Lett. **23**, 558–560 (2011).
24. R. Slavic and S. LaRochelle, "Large-band periodic filters for DWDM using multiple-superimposed fiber Bragg gratings," IEEE Photon. Technol. Lett. **14**, 1704-1706 (2002).
25. A. Dupuis, J. F. Allard, D. Morris, K. Stoeffler, C. Dubois, M. Skorobogatiy, "Fabrication and THz loss measurements of porous subwavelength fibers using a directional coupler method," Opt. Express **17**, 8012 (2009).
26. G. Yan, A. Markov, Y. Chinifooroshan, S. M. Tripathi, W. J. Bock, and M. Skorobogatiy, "Resonant THz sensor for paper quality monitoring using THz fiber Bragg gratings," Opt. Lett. **38**, 2200-2202 (2013).
27. M. Shalaby, M. Peccianti, Y. Ozturk, M. Clerici, I. Al-Naib, L. Razzari, T. Ozaki, A. Mazhorova, M. Skorobogatiy, and R. Morandotti, "Terahertz Faraday rotation in a magnetic liquid: High magneto-optical figure of merit and broadband operation in a ferrofluid," Appl. Phys. Lett. **100**, 241107 (2012).
28. S. Pandey, B. Gupta, and A. Nahata, "Terahertz plasmonic waveguides created via 3D printing," Opt. Express **21**, 24422-24430 (2013).
29. S. F. Busch, M. Weidenbach, M. Fey, F. Schäfer, T. Probst, and M. Koch, "Optical Properties of 3D Printable Plastics in the THz Regime and their Application for 3D Printed THz Optics," J. Infrared Millim. Terahertz Waves **35**, 993-997 (2014).
30. D. W. Vogt, J. Anthony, and R. Leonhardt, "Metallic and 3D-printed dielectric helical terahertz waveguides," Opt. Express **23**, 33359-33369 (2015).
31. J. D. Jackson, *Classical Electrodynamics* (John Wiley, 1999).
32. T. Hattori, R. Rungsawang, K. Ohta and K. Tukamoto, "Gaussian Beam Analysis of Temporal Waveform of Focused Terahertz Pulses," J. Appl. Phys. **41**, 5198-5204 (2002).
33. E. J. Kowalski, M. A. Shapiro, R. J. Temkin, "Simple correctors for elimination of high-order modes in corrugated waveguide transmission lines," IEEE Trans. Plasma Sci. **42**, 29-37 (2014).
34. C. D. Poole, J. M. Wiesenfeld, A. R. McCormick, and K. T. Nelson, "Broadband dispersion compensation by using the higher-order spatial mode in a two-mode fiber," Opt. Lett. **17**, 985-987 (1991).
35. N. M. Litchinitser, B. J. Eggleton, and D. B. Patterson, "Fiber Bragg gratings for dispersion compensation in transmission: theoretical model and design criteria for nearly ideal pulse recompression," IEEE J. Lightwave Technol. **15,** 1303-1313 (1997).
36. T. Nagatsuma, G. Ducournau, and C. C. Renaud, "Advances in terahertz communications accelerated by photonics," Nature Photon. **10**, 371–379 (2016).
37. S. Jiang, E. Newton, C. Yuen, and C. Kan, "Chemical silver plating on cotton and polyester fabrics and its application on fabric design, Text. Res. J. **76,** 57–65 (2006).
38. M. Skorobogatiy, *Nanostructured and Subwavelength Waveguides: fundamentals and applications*, (Wiley, 2012)
39. H. H. Rose, *Geometrical Charged-Particle Optics*, (Springer, 2009).
40. A. Roggenbuck, K. Thirunavukkuarasu, H. Schmitz, J. Marx, A. Deninger, I. C. Mayorga, R. Güsten, J. Hemberger, and M. Grüninger, "Using a fiber stretcher as a fast phase modulator in a continuous wave terahertz spectrometer," J. Opt. Soc. Am. B **29**, 614-620 (2012).
41. J. Suen, M. Fang, S. Denny, and P. Lubin, "Modeling of Terabit Geostationary Terahertz Satellite Links From Globally Dry Locations," IEEE Trans. Terahz Sci. Technol. **5**, 299–313 (2015)

1. Introduction

With the demand of wider bandwidths and higher bit rates, using terahertz frequencies for wireless communications is experiencing a surge of attention in recent years. Various THz

Optics EXPRESS

wireless communication systems with carrier frequencies as high as 0.6THz and transmission data rates of up to 100Gbit/s have been developed and investigated [1-4]. However, applications of these THz communication systems are still limited due to inherent challenges posed by the free space propagation (FSP) modality, such as strong dependence on atmospheric conditions, rapid divergence of the THz beams especially at the lower carrier frequencies, as well as line-of-sight nature of the links. Particularly, due to self-diffraction and THz relatively long wavelength $\sim 1\text{mm}$, realizing low divergent THz beams requires the use of large beam diameters and focusing optics that can be as big as several tens of centimeter in diameter for even short communication links of several tens of meters. Additionally, due to strong directionality of the THz beams, wireless communications access to partially blocked areas can be problematic, thus, requiring additional THz steering solutions for reliable communications.

At the same time, low-loss terahertz fibers and waveguides offer good solutions to some of the limitations caused by the free space THz propagation, and can have their own niche applications in THz communications. There are some clear advantages of using THz waveguides and fibers. Particularly, as light propagates through sealed THz fibers, influence of the atmospheric conditions on the communication link quality is minimized. Additionally, THz fibers are flexible and of small diameters, hence, allowing access to otherwise physically obstructed areas. Finally, THz fiber size is typically comparable to the wavelength of light, thus enabling compact several-mm in diameter communication links with very small footprint and low signal leakage outside of the fibers, which is of special interest for the ultra-high bandwidth on-chip interconnects. In the past decade, various THz fibers with low transmission losses ($<0.01\text{cm}^{-1}$) have been proposed and demonstrated. Generally, such waveguides maximize the fraction of the guided power in the low-loss gas [5-15]. Among these designs, one generally distinguishes subwavelength THz fibers that guide using total internal reflection (TIR) mechanism [5-8] and hollow core fibers that guide using either photonic bandgap confinement [9-13] or anti-resonant reflection (ARROW) [14,15].

While loss reduction in THz fibers can be considered as a solved problem, fiber dispersion management remains generally an unsolved problem. In free space systems, Group Velocity Dispersion (GVD) of transmission media results in the temporal broadening of the THz pulses that are typically generated using THz-TDS (Time Domain Spectroscopy) systems. In the fiber-based communication systems, modal GVD similarly leads to pulse broadening, and hence reduction in the maximal bit rate supported by the fiber communication link of fixed length. This happens because adjacent "bits" of temporal size Δt in the pulse train broaden and become $\widetilde{\Delta t}$ after propagation over length L in the fibers with GVD D, as $\Delta \tilde{t} \sim L \cdot D / \Delta t$. One considers that the pulse train gets scrambled when adjacent "bits" overlap which happens for the "bits" of temporal duration shorter than $\Delta t \le \sqrt{D \cdot L}$. As detailed in Ref. [16], the dispersion-limited maximum bitrate can be given as $B_m = 1/(4\sqrt{D \cdot L})$. For example, considering a typical THz fiber dispersion of $D \sim 1$ *ps/(THz•cm)*, in order to obtain even a moderate bit rate of 10Gbit/s, the maximum transmission length is limited to ~6 m. On the other hand, transmission rates of $100\ \text{Gbit/s}$ would limit transmission links to only 6 cm with standard THz waveguides.

Note that even in the wireless links, where dispersion of dry air at THz frequencies is relatively small $D \sim 2.5 \times 10^{-4}$ *ps/(THz•cm)* [17], wireless link length will still be limited due to pulse dispersion. For example, for a wireless link of length 250 m, the maximal bitrate supported by such a link without dispersion compensation will be 100 Gbit/s. In addition to pulse distortion due to group velocity dispersion, frequency dependent absorption loss due to water vapor will further contribute to pulse distortion, and in some cases one might prefer using fiber-based THz links over free space THz links as a backup option for reliability considerations (for example, when consistent performance is required at any weather conditions). Overall, while effects of dispersion on signal degradation appear modest in the free space links, they are a major limiting factor in the waveguide-based interconnects, and therefore should be further addressed and mitigated.

Optics EXPRESS

A straightforward way of reducing the GVD of a THz waveguide link is via a judicial design of the waveguide geometry. For example, in our previous work [8], we have demonstrated an effectively graded index porous THz fiber incorporating an air-hole array of variable air-hole diameters and inter-hole spacing. Compared to the porous THz fiber featuring regular air-hole array, the graded index fiber successfully reduced both the individual modal and intermodal dispersions. Further reduction of the GVD below 0.1*ps/(THz•cm)*, however, proved to be challenging and there are only few examples in the literature of such THz waveguides [18].

In order to address the issue of pulse dispersion, one can pursue an alternative approach. Thus, instead of reducing GVD of a transmission link, one can rather use dispersion compensation at the link end, or dispersion pre-compensation at the beginning of the link. There are several requirements for these effective dispersion compensation systems. First is efficient coupling between the transmission fiber and the dispersion compensating waveguide. Second is a single mode operation of both the transmission fiber and dispersion compensating waveguide, in order to avoid multimode interference effects and intermodal dispersion. Third is the requirement of the high negative dispersion of the dispersion compensating waveguide D_{DCW} in order to compensate with a short device length L_{DCW} for the positive dispersion D_L incurred over a transmission link of length L_L so that $D_{DCW} \cdot L_{DCW} + D_L \cdot L_L = 0$, and $L_{DCW} \ll L_L$ [19]. Finally, dispersion compensation condition has to be satisfied over a wide enough frequency range comparable to the communication signal bandwidth.

We note that, several on-chip devices based on parallel plate THz waveguides or spoof-plasmon modes propagating between planar interfaces have been reported for the dispersion control in the THz domain. For example, T. Fobbe et al. [20] proposed a hybrid waveguide made by connecting a dielectric-metal and a metal-metal parallel plate waveguides. This resulted in a broadband tunable THz device offering a small negative GVD on the order of tens of $ps/(THz \cdot cm)$. Meanwhile, Gao et al. [21] used a graded plasmonic resonator chain for the dispersion control in the microwave range. The authors theoretically predicted that localized spoof surface plasmon polaritons in the resonator chain provide both positive and negative dispersion that can be easily tailored by tuning the structural parameters. In the abovementioned works, however, the authors did not consider the tradeoff between the bandwidth and the value of the GVD, which is important and indispensable for practical applications. Moreover, for both proposed waveguides, the coupling efficiencies with the external THz beam are not studied. Indeed, the use of a planar geometry suggests low coupling efficiencies in the absence of mode converters, which would further limit practical applications of such devices.

In our paper, we pursue a different approach. Particularly, we aim at designing a waveguide-based dispersion compensator with the highest negative dispersion possible, while keeping its operational bandwidth large enough to support THz wireless communications (5-10*GHz*). This design approach leads to shorter devices, and, therefore, lower propagation losses are expected compared to devices with smaller GVDs. Being hollow and circularly symmetric, our waveguides are inherently suitable for operation with the free space beams. Thus, we expect much higher coupling efficiencies for our devices and lower modal propagation losses compared to those of devices based on planar geometries. Furthermore, we present a discussion of the tradeoff between the waveguide GVD value and the device bandwidth. Finally, we present several strategies aimed at increasing the excitation efficiency of our waveguides with a free-space Gaussian beam, while keeping a single mode operation.

While focusing on the problem of dispersion compensation in the THz communication links, we recognize that this is a part of a much broader research area of analog signal processing in the THz spectral range. Analog signal processing is, in fact, a very active research area in the near-IR spectral range where most of the optic communication systems are developed, while in THz this subject is steadily gaining its recognition. In the near-IR one of the key enabling devices for analog signal processing is a chirped Fiber Bragg Grating (FBG) that operates in the reflection mode. Used in combination with fiber couplers and fiber optic

circulators, chirped FBGs can be used to perform a variety of signal processing operations including dispersion compensation [22], signal modulation [23], wavelength division multiplexing [24], to name a few. Unfortunately, in the THz spectral range, there are only few examples to date of the advanced waveguide components that are required for building analog signal processing devices using waveguide Bragg gratings (WBGs) in the reflection mode. While, some of the THz components have been demonstrated such as couplers [25] and FBGs [26], others like circulators have only being partially developed [27]. Therefore, in our study of the dispersion compensation in the THz range we resort to the use of waveguide Bragg gratings operating in the transmission mode (rather than reflection mode), which are considerably simpler to integrate into a communication link. Moreover, in order to mitigate relatively high losses of the materials in the THz spectral range, we use hollow core waveguides in our designs of the dispersion compensating WBG devices.

In this paper, we explore theoretically and experimentally two novel waveguide Bragg gratings (WBGs) operating in the transmission mode. The goal is to demonstrate the WBG-based devices capable of dispersion compensation in THz communication links that operate in a single mode regime, have high negative dispersions, and show high coupling efficiency to the incoming linearly polarized Gaussian beam.

The proposed WBGs were first fabricated from photosensitive resins using 3D stereolithography, which is a highly versatile and robust technique for the fabrication of optical devices at terahertz frequencies [13, 28-30]. Subsequently, the printed devices were metalized with silver nanolayers using the wet chemistry approach. Optical properties of the fabricated WBGs were then investigated numerically using the finite element method, as well as experimentally using both the continuous-wave terahertz (CW-THz) spectroscopy and terahertz time-domain spectroscopy (THz-TDS) imaging. The results confirm both single mode operation and large negative dispersion for both fabricated WBGs near 140GHz. Specifically, for the first WBG, the single mode operation is attainable over the frequency range of 138-146GHz, where the dispersion varies between -467 and -191 $[ps/(THz \cdot cm)]$. Meanwhile, for the second WBG, we achieve a single mode operation range between 137-142GHz, where the dispersion is in the range of -330 and -138 $[ps/(THz \cdot cm)]$.

2. Dispersion compensation strategies using modes of a hollow core waveguide

As discussed in the introduction, for the efficient dispersion compensation, several requirements should be satisfied by the dispersion compensating device, including efficient excitation, single mode operation, large negative dispersion, and sizable bandwidth. At THz wavelengths, some of these conditions can be satisfied using the large diameter metallic tubes that can show excellent coupling with a focused THz beam and high value of the negative GVD near the modal cut-off frequencies. In Fig. 1(a), we schematically show dispersion relations of the fundamental mode and the first higher order mode of a circular metallic tube, where ω_c^1 and ω_c^2 are the cutoff frequencies for the fundamental mode (red line) and the first higher order mode (blue line). For frequencies between ω_c^1 and ω_c^2, metallic tube supports a single mode guidance with negative dispersion (gray region in Fig. 1(a)). As optical characteristics of the metallic tubes are strongly dependent on their core size, one should consider trade-offs between the core size and the value of the negative dispersion, as well as single mode versus multimode operation, when using such waveguides for dispersion compensation. For example, the dispersion relation of guided modes in a metal tube of radius r is given by [31]:

$$\beta_{mn} = \frac{1}{c}\sqrt{\omega^2 - \left(\omega_c^{mn}\right)^2} \tag{1}$$

where $\omega_c^{mn} = X_{mn}c/r$ is the modal cutoff frequency, and X_{mn} is the n-th nonvanishing root of the m-th order second kind Bessel function $Y_m(\omega)$ (for TE modes) or the m-th order first kind Bessel function $J_m(\omega)$ (for TM modes). If λ is the operational wavelength, single mode regime is realized for the tube radii of $0.29\lambda < r < 0.38\lambda$. A typical beam waist size of the focused

Optics EXPRESS

diffraction limited THz Gaussian beam is $w_0 \sim 4\lambda f/(\pi D)$ [32], where f and D are the focal distance and diameter of the focusing lens, respectively, with field intensity dependent as $|E|^2 \propto \exp[-2r^2/{w_0}^2]$. In our system, we use $f = 2D = 10\text{cm}$, thus resulting in the Gaussian beam waste size of $w_0 \sim 2\lambda$. Moreover, we note that in general, high quality THz parabolic mirrors and lenses that are currently available commercially feature $f/D \gtrsim 1$ ratios, which is inherent to the design of classical focusing optics. Therefore, resultant Gaussian waist size is typically larger than $1 - 2\ \lambda$ for any choice of the standard focusing optics. We note, that in order to achieve efficient coupling to the fundamental HE_{11} mode, the tube size has to be larger than the Gaussian beam size, namely $r \approx 1.5w_0$ [33]. However, when trying to operate near the first cutoff frequency (region of high negative dispersion), the tube radius should be $r \approx 0.29\lambda \ll w_0 \approx 2\lambda$, which leads to inefficient coupling between the focused Gaussian beam and the tube fundamental mode near its cutoff frequency. In order to increase the coupling efficiency between the focused Gaussian beam and the fundamental mode of a tube, one needs either to increase the tube diameter or, equivalently, increase the operational frequency. For instance, in the case of a Gaussian beam with a waist of 2λ, the coupling efficiency is optimal and equal to (96%) if the tube size is $r = 2.93\lambda$. However, at this frequency, the number of $m = 1$ modes supported by the tube will be 12 and the propagation regime is multimode.

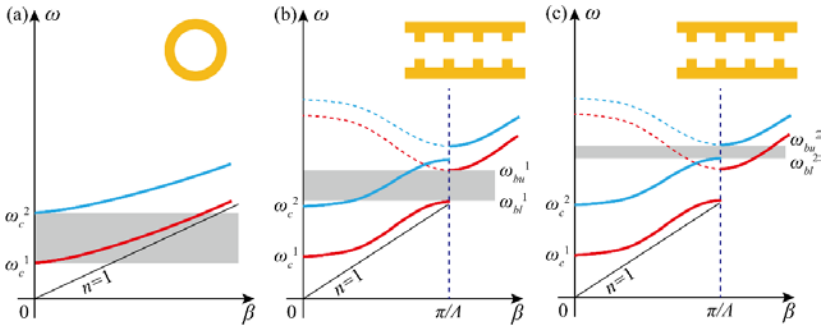

Fig. 1. Schematics of the dispersion relations for the few lowest order modes in (a) metal tube waveguide, (b) and (c) metal tubes waveguide with periodic corrugations. In gray, we show spectral regions of single mode operation and negative modal dispersion. Black line: light line of air. Red curve: the fundamental mode. Blue curve: a higher order mode.

In order to promote higher coupling efficiency, while maintaining high negative dispersion and single mode operation, we pursue two complimentary approaches that are similar in spirit to those described in [34, 35]. One is to use a higher order mode that is compatible in symmetry with a linearly polarized Gaussian beam (HE_{12}, for example), while operating in the vicinity of its cut-off frequency ω_c^2. At the same time, in order to guarantee single mode operation, we have to suppress coupling to the fundamental HE_{11} mode. This can be achieved by introducing periodic corrugation into the tube inner core, while opening a bandgap (frequency range from ω_{bl}^1 to ω_{bu}^1 shown in gray in Fig. 1(b)) for the fundamental HE_{11} mode in the vicinity of the HE_{12} cut-off frequency ω_c^2. Alternatively, one can open a bandgap for the higher order mode HE_{12} [frequency range from ω_{bl}^2 to ω_{bu}^2 shown in gray in Fig. 1(c)], while operating in the vicinity of the upper bandgap edge of the fundamental mode ω_{bu}^1. In this case, the waveguide is again single mode, operation at higher frequencies allows better mode matching between the focused Gaussian beam and the fundamental HE_{11} mode, and finally, strong negative dispersion is achieved due to operation close to the upper bandgap edge of the fundamental mode.

Particularly, in the first WBG1, we implement the scenario highlighted in Fig. 1(b), where single mode operation is using the HE_{12} mode operating in the vicinity of it cutoff frequency, while guidance in the fundamental HE11 mode is suppressed due to the bandgap effect. In the second WBG2 we realize the scenario highlighted in Fig. 1(c), where single mode operation is using the fundamental HE_{11} mode operating in the vicinity of the corresponding upper bandgap

Optics EXPRESS

edge, while guidance in the fundamental HE_{12} mode is suppressed due to the bandgap effect. Both WBGs are designed and optimized for the dispersion compensation in the vicinity of the operation frequency of ~140GHz. This particular choice for the operation frequency is dictated by the relatively low atmospheric absorption at such frequencies (atmospheric transparency window), as well as commercial availability of the high-power THz sources and detectors that will be used in the first-generation THz communication systems [36].

Successful application of the dispersion compensation fibers in the THz communication links also requires that the GVD of the dispersion compensation fiber remains constant over the signal bandwidth. Otherwise, problems caused by the higher order dispersion can be pronounced [23]. Here, we explore briefly the relation between the value of GVD and the operation bandwidth for the dispersion compensating fibers operating either in the vicinity of the modal cutoff frequency (WBG1) or in the vicinity of the bandgap edge (WBG2).

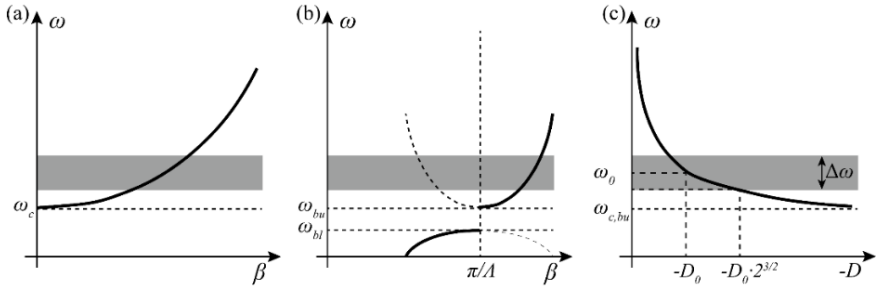

Fig. 2. Schematics of the dispersion relations for (a) the mode operating close to its cut-off frequency ω_c and (b) the mode operating close to its upper bandgap edge ω_{bu}. (c) Schematic of the corresponding modal GVD. In gray: the spectral bands used for the dispersion compensation, they are centered at ω_0 and have a bandwidth of $\Delta\omega$.

For the first waveguide Bragg grating (WBG1), we use the first higher order mode HE_{12} compatible in symmetry with the linearly polarized Gaussian beam for the dispersion compensation, and operate in the frequency range close to the HE_{12} cut-off frequency [shown in gray in Fig. 2(a)]. The GVD of the HE_{12} mode can be derived from its modal dispersion relationship (Eq. 1) as:

$$D_{WBG1} = \frac{\partial^2 \beta}{\partial \omega^2} = -\frac{1}{c}\frac{\omega_c^2}{\left[\omega^2 - \omega_c^2\right]^{3/2}} \tag{2}$$

On the other hand, the second waveguide Bragg grating (WBG2) is operated in the frequency range close to the upper bandgap edge of the fundamental (HE_{11}) mode [shown in gray in Fig. 2(b)]. In this frequency range, the dispersion relation of the mode can be approximated as $\beta = \frac{\pi}{\Lambda} + \frac{1}{\gamma c}\sqrt{\omega^2 - \omega_{bu}^2}$, where Λ is the periodicity of corrugation and γ is a certain coefficient. The GVD of the fundamental HE_{11} mode can then be approximated as:

$$D_{WBG2} = \frac{\partial^2 \beta}{\partial \omega^2} = -\frac{1}{\kappa c}\frac{\omega_{bu}^2}{\left[\omega^2 - \omega_{bu}^2\right]^{3/2}} \tag{3}$$

where ω_b is the upper edge of the bandgap for the fundamental (HE_{11}) mode.

In general, we define the bandwidth $\Delta\omega$ as a frequency range centered at ω_0 within which the dispersion changes at most by a factor of x, namely $D(\omega_0 - \Delta\omega/2) = x \cdot D_0$. Here, $D_0 = D(\omega_0)$ is the value of the dispersion at the central (carrier) frequency, and x is a certain design parameter dictated by the specifications of the communication system. In this paper, we chose $x = 2^{3/2} \sim 2.83$ as this choice results in a simple expression for the relation between the desired dispersion D_0 and the bandwidth $\Delta\omega$, which is given by:

Optics EXPRESS

$$D(\omega_0 - \Delta\omega/2) = 2^{3/2} D_0$$
$$D_0 \approx \left(\frac{\omega_*}{c\Delta\omega^3}\right)^{1/2} \quad (4)$$

where $\omega_* = \omega_c$ for the WBG1, while $\omega_* = \omega_{bu}$ for the WBG2 [see Fig. 2(c)]. In our derivations, we assumed that $\Delta\omega \ll \omega_0, \omega_c, \omega_{bu}$, which is indeed the case for the proposed waveguide Bragg gratings as the dispersion compensation is done at frequencies ~140GHz, while the desired bandwidth is ~10GHz. Finally, from Eq. (4) it follows the estimate for the maximal dispersion of the dispersion compensation waveguide WBG1 or WBG2 operating at ~140GHz and having ~10GHz bandwidth is $D_0 \approx -1985\text{ps}/(\text{THz}\cdot\text{cm})$.

3. Fabrication of the waveguide Bragg gratings

The proposed waveguide Bragg gratings are realized by introducing triangular steps inside of a hollow core tube. Both Bragg gratings comprise 40 periodically arranged triangular steps. The shape of the steps is chosen for the ease of 3D printing. The 3D model of the proposed waveguide Bragg gratings is shown in Fig. 3(a). The structural parameters, including the tube core diameter *D*, the base size *p* and the height *h* of triangular steps, were optimized to enable effectively single mode propagation and large negative dispersion of a chosen guided mode (HE_{11} or HE_{12}) in the vicinity of 0.14THz, as detailed in the following sections. For the sake of comparison, we also fabricated hollow core waveguides (without corrugation) with the same core diameters and total lengths as those of the corresponding waveguide Bragg gratings. The prototypes of all the aforementioned waveguides were fabricated using a stereolithography 3D printer (*Asiga® Freeform PRO2*) with the photosensitive resin (*PlasCLEAR*). The printer has a resolution of 50μm along the x- and y-axes, and 1μm along the z-axis. Subsequently, the printed prototypes were cleaned and immersed into isopropanol solution for ~12hrs, and then fully coated with a silver layer using a wet chemistry coating method as detailed in [37].

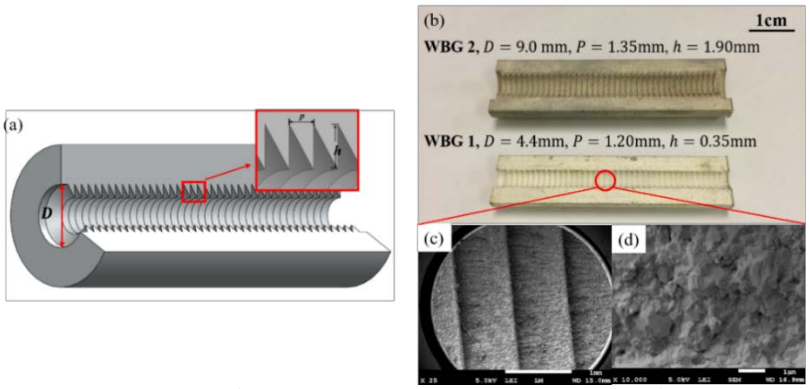

Fig. 3. (a) 3D schematic of the waveguide Bragg grating. Insert: zoom of the grating. (b) Dissected waveguide Bragg gratings 1 and 2. (c) and (d) SEM images of the area highlighted by the red circle in (b) with magnifications of ×25 and ×10000, respectively.

The fabricated waveguide Bragg gratings are shown in Fig. 3(b) (only one half of the dissected waveguides are shown). The surface of the periodic corrugations was imaged using a scanning electron microscope (SEM). As shown in the SEM images [Fig. 3(c) and 3(d)], the wet chemistry coating produces a uniform deposition of silver particles on the waveguide surface. The grain size of the silver particles varies from hundreds of nanometers to several micrometers. Resulting silver layer has thickness which is much larger than the skin depth for the THz waves (≤ 100nm) which prevents them from leaking into the dielectric cladding. As roughness of the coated silver layer ($\sim$1μm) is deeply subwavelength (THz wavelength is $\sim$1mm), thus only a small scattering loss is expected due to surface roughness, which we have

Optics EXPRESS

confirmed experimentally by comparing transmission through Ag-coated tubes and polished copper tubes.

4. Numerical modeling

Light guidance in the proposed waveguide Bragg gratings was first analyzed numerically using COMSOL finite element software. The computation cell is that of the unit cell of an infinitely periodic structure corresponding to the grating under study. In the transverse direction, the unit cell is terminated by a perfect electric conductor that simulates the air/metal interface. In the longitudinal direction, Bloch-Floquet boundary condition is used. In Fig. 4, we demonstrate the computed band diagrams for the two waveguide Bragg gratings shown in Fig. 3(b). The color code for the modal dispersion relations corresponds to the absolute value of the modal coupling coefficient to the 3D Gaussian beam focused into the center of the WBG input facet. The coupling coefficients are computed using continuity of the transverse electric field components across the coupling interface between the incident Gaussian beam and the guided modes [38]:

$$C_m = \frac{\iint \left(\boldsymbol{E}_m^* \times \boldsymbol{H}_{in} + \boldsymbol{E}_{in} \times \boldsymbol{H}_m^* \right) drdz}{2\sqrt{\iint \mathrm{Re}\left(\boldsymbol{E}_m^* \times \boldsymbol{H}_m \right) drdz} \times \sqrt{\iint \mathrm{Re}\left(\boldsymbol{E}_{in}^* \times \boldsymbol{H}_{in} \right) drdz}} \tag{5}$$

where integration is performed over the whole unit cell. Field distribution in the linearly polarized 3D Gaussian beam is given by [39]:

$$\boldsymbol{E}_{in}(r,z) = \vec{\boldsymbol{y}} \cdot \exp\left(-\left(r/w_0 \right)^2 \right) \cdot \exp\left(-ikz \right) \tag{6}$$

where w_0 is the beam waist size (radius). The Gaussian beam waist size is dependent both on the frequency of THz light and the focusing optics so that $w_0 = 4\lambda f/(\pi D)$, where f and D are the focal length and the diameter of the parabolic mirror (or a lens) used for beam focusing. In our CW-THz experimental setup discusses in section 5, f*=10 cm* and *D=5 cm*, and the beam waist radius is estimated to be $w_0 \sim 2\lambda$. Magnetic field of the external Gaussian beam can be calculated from Eq. 5 using one of the Maxwell equations, $\boldsymbol{B}_{in} = \frac{i}{\omega} \nabla \times \boldsymbol{E}_{in}$.

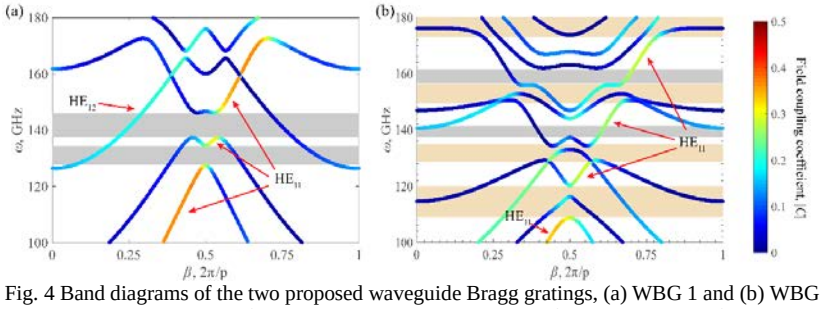

Fig. 4 Band diagrams of the two proposed waveguide Bragg gratings, (a) WBG 1 and (b) WBG 2 shown in Fig. 3. Color of the modal dispersion relations refers to the value of the modal coupling coefficient to the focused Gaussian beam with the beam waist of $w_0 \sim 2\lambda$. Gray regions correspond to the spectral ranges where WBGs are effectively single mode. Beige regions refer to the bandgaps of the fundamental HE_{11} mode.

In Fig. 4, we present modal dispersion relations of the guided modes with angular momentum equal to 1 ($m = 1$). Modes with other angular momenta would not be excited by a centrally coupled, linearly polarized Gaussian beam due to symmetry mismatch. For clarity of presentation, in Fig. 4 we only present modes with coupling coefficients higher than 0.01. We design WBG1 to operate in the single mode regime using the HE_{12} mode for the dispersion compensation. The geometrical parameters that we use for WBG1 are $D = 4.4\mathrm{mm}$, $P = 1.20\mathrm{mm}$, and $h = 0.35\mathrm{mm}$. From Fig. 4(a) we observe two spectral regions of the effectively single mode guidance (shown in gray) which are 127.6-134.4 GHz and 137.5-146.0GHz. Note that strictly speaking, within these two frequency ranges there are two modes that can

Optics EXPRESS

propagate. However, the coupling coefficient is virtually zero for one of the two modes as it corresponds to the backward propagating mode. In these frequency ranges, as shown in more details in Fig. 5(b), the dispersion of the HE_{12} mode varies between -13360 and $-780\ [\mathrm{ps/(THz\cdot cm)}]$ and -467 and $-191\ [\mathrm{ps/(THz\cdot cm)}]$ respectively. Using criterion (4) we conclude that the operation wavelengths, dispersion values and the maximal bandwidths of the dispersion compensator WBG1 are $\omega_0 = 131.5\mathrm{GHz}, D_0 = -1568\mathrm{ps/(THz\cdot cm)}, \Delta\omega = 5.2\mathrm{GHz}$, and $\omega_0 = 141.6\mathrm{GHz}, D_0 = -268.6\mathrm{GHz}, \Delta\omega = 8.5\mathrm{GHz}$ respectively. In Figs. 5 (c) and 5(d) we present longitudinal flux distributions S_z of the HE_{12} mode at 130GHz and 140 GHz. By observing the modal distribution, we confirm that the mode used for dispersion compensation is similar to the HE_{12} mode of a simple tube, and it remains unaffected by other guided modes and plasmonic excitations within the frequency range of interest.

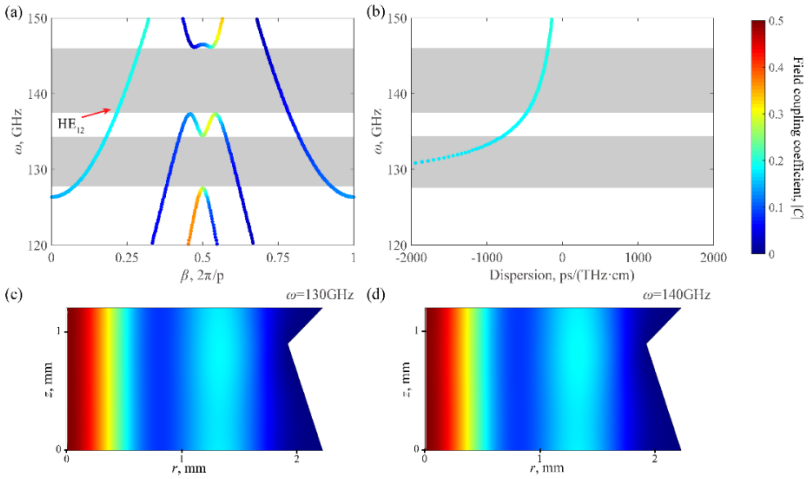

Fig. 5 Dispersion compensator WBG1. (a) Dispersion relations of the guided modes and (b) HE_{12} mode group velocity dispersions within the spectral regions of the effective single mode guidance (gray regions) in the vicinity of 130GHz and 140 GHz. (c), (d) Longitudinal flux distributions S_z of the HE_{12} mode at 130GHz and 140 GHz.

Next, we design WBG2 to operate within bandgaps of the higher order modes, where waveguide can be considered effectively single mode with maximal coupling coefficient to the HE_{11}-like mode. The geometrical parameters that we use for WBG2 are $D = 9.0$ mm, $P = 1.35\mathrm{mm}$, and $h = 1.90\mathrm{mm}$. From Fig. 4(b), we observe that there are two spectral regions of the effectively single mode operation. One is in the vicinity of 140 GHz, while another one is in the vicinity of 160 GHz. Unlike the case of WBG1, both positive and negative dispersions are possible for the WBG2, as shown in Fig. 6(b). This is caused by avoiding crossing with the higher order modes (including plasmonic modes). In Fig. 6(c) and 6(d), we present longitudinal flux distributions S_z of the HE_{11}-like mode at two frequencies labelled by red circles and the letters A and B in Fig. 6(a). Obviously, the fundamental mode of WBG2 is a HE_{11}-like mode at 147GHz, while it is decorated with the plasmonic excitation present near the metal surface at 137GHz. In fact, these plasmonic excitations can significantly modify the dispersion relation of the core guided modes (such as the fundamental HE_{11} mode) via the phenomenon of avoided crossing as evidenced from Fig. 6. In this paper, we do not explore the regime of the hybridized core guided / plasmonic modes, mainly for the reason that in this particular example although the resultant negative dispersion can be extremely high, the bandwidth of operation is limited. That said, we believe that hybridized core guided / plasmonic modes have strong potential in dispersion compensation, and they will be studied in more details in our following works.

Optics EXPRESS

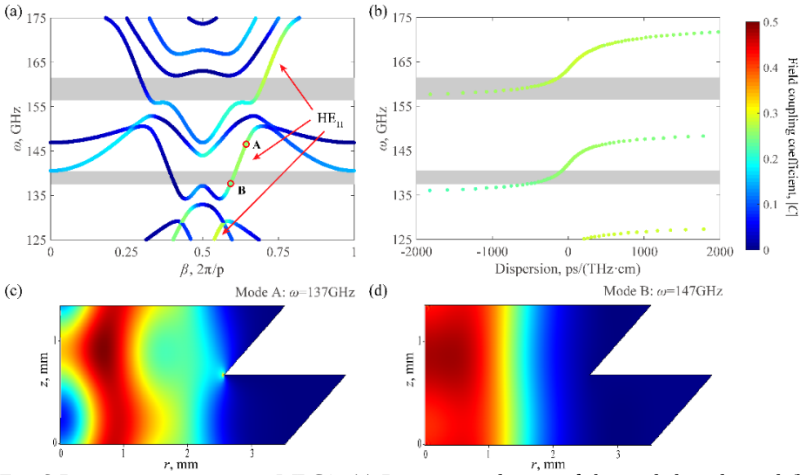

Fig. 6 Dispersion compensator WBG2. (a) Dispersion relations of the guided modes and (b) HE_{11} mode group velocity dispersions within the spectral regions of the effective single mode guidance (gray regions) in the vicinity of 140 GHz and 160 GHz. (c) and (d) Longitudinal flux distributions S_z of various guided modes labelled by red circles in (a).

In the spectral ranges of single mode guidance of the fundamental HE_{11}-like mode in the vicinity of 140GHz and 160GHz, mode dispersions are negative and vary strongly. Thus, in the range of 137.5-140.5GHz (gray region at the bottom of Fig. 6(b)), the dispersion varies between -330 and -138 $[\mathrm{ps}/(\mathrm{THz}\cdot\mathrm{cm})]$. For frequencies within this range, all the higher order modes are eliminated due to bandgap effects, and only the fundamental HE_{11}-like mode remains. At the same time, in this frequency range the modal dispersion value changes markedly, therefore, the problem of increasing the operational bandwidth by keeping the dispersion value relatively constant still deserves further study. Similarly, in the vicinity of 160 GHz, the single mode guidance is realized over 156.5-161.5GHz, where the dispersion changes from -9832 $[\mathrm{ps}/(\mathrm{THz}\cdot\mathrm{cm})]$ to -130 $[\mathrm{ps}/(\mathrm{THz}\cdot\mathrm{cm})]$. Using criterion (4a) we conclude that the operation wavelengths, dispersion values and the maximal bandwidths of the dispersion compensator WBG2 are $\omega_0 = 139.0\mathrm{GHz}$, $D_0 = -217.8\mathrm{ps}/(\mathrm{THz}\cdot\mathrm{cm})$, $\Delta\omega = 3.0\mathrm{GHz}$, and $\omega_0 = 160.2\mathrm{GHz}$, $D_0 = -291.5\mathrm{ps}/(\mathrm{THz}\cdot\mathrm{cm})$, $\Delta\omega = 2.8\mathrm{GHz}$.

5. Optical characterization of the waveguide Bragg gratings

5.1 Transmission measurements

Optical characterization of the fabricated waveguides was carried out using continuous wave Terahertz (CW-THz) spectroscopy system (*Toptica* Photonics) shown schematically in Fig. 7. The setup has two distributed feedback (DFB) lasers with slightly different center wavelengths and a uniform power (~30mW each) operating in the telecom region. A 50:50 coupler combines and splits the two wavelengths equally into the emitter and detector arms respectively. The beat signal of the two lasers is split into two beams by the fiber coupler and then delivered to the emitting and detecting antennas using two single mode polarization maintaining fibers. Two fiber stretchers, which are driven by the piezo actuators and stretched in the opposite directions, are connected to both arms. The detected signal is a photocurrent I_{ph}, which depends both on the amplitude $|E_{THz}|$ of the measured terahertz electric field and on the phase difference $\Delta\varphi$ between the two optical beams [40]:

$$I_{ph} \propto |E_{THz}| \cdot \cos(\Delta\varphi) = |E_{THz}| \cdot \cos(2\pi\Delta L\nu/c + \varphi_0) \tag{7}$$

where ΔL denotes the optical path difference between the transmitter arm and the receiver arm, while φ_0 denotes the phase difference between the two arms for a neutral position of the stretcher. The optical path length ΔL is varied in a predefined fashion using fiber stretchers, which allows extraction of the field amplitude and phase by fitting periodic modulation in the

Optics EXPRESS

measured photocurrent using Eq. (7). The symmetric arrangement of the fiber stretchers provides additional path delay as well as phase noise cancelation that can be caused by the variation in the environment. The path lengths between the emitter and the detector arms are balanced (in the empty configuration) to have a flat frequency independent phase. The THz waves are generated by the emitter photomixer which emits the frequency difference between the two lasers which are furthermore modulated using the bias voltage for lock-in detection. By tuning the lasing wavelengths, such a system can generate a tunable THz radiation in the range of 50 GHz-1.2 THz, with bandwidth as narrow as 40MHz. The THz beams were focused into and collected from the waveguides using the gold coated reflective optics (flat and parabolic mirrors). Two metallic apertures were placed at the input and output facets of the waveguide to block any stray light and avoid coupling into plastic cladding. The measurements were obtained in the frequency range 100-180GHz with 100MHz frequency resolution and 600ms integration time constant. The generated photocurrent in the detector was recorded along with the phase information as a function of frequency.

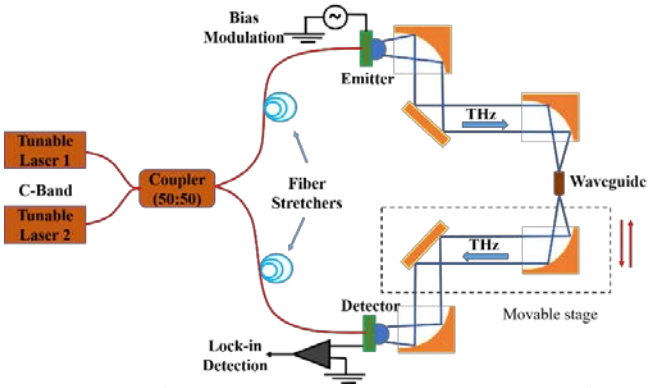

Fig.7 Schematic of the CW-THz setup for optical characterization of WBGs.

The measured THz electric fields and the corresponding transmission spectra for the two fabricated waveguide Bragg gratings (red curves), metalized tube and copper tube (blue and magenta curves) are shown in Fig. 8. The references (black curves) were acquired by removing the measured waveguides, while displacing one set of the parabolic mirrors to share the focal plane with that of the second stationary parabolic mirror. Additionally, at the focal point, we used an aperture with an opening similar to the core size of the measured waveguide. The measured reference photocurrent shows the prominent standing wave with beat frequency of 4 GHz, which is due to the Fabry–Pérot interference within the silicon lenses of the photomixers. The complex transmission coefficient through a waveguide is:

$$T(\omega) = E_t / E_r = t(\omega) \cdot \exp\left(i\varphi(\omega)\right) \tag{8}$$

where E_t and E_r are the complex electric fields measured with and without the tested waveguide, $t(\omega)$ is the transmission amplitude, while $\varphi(\omega)$ is the phase.

Firstly, we characterized the performance of the metalized 3D printed tube, and compare it with that of the commercial copper tube of the same core size and length. As seen in Fig. 8 (d), the metalized tube feature very similar transmission spectrum as that of the commercial copper tube in the frequency range of 100-180GHz. From this, we conclude that our metallization recipe was chosen correctly.

Next, we characterize transmission through the fabricated waveguide Bragg gratings. For the WBG1 [left column in Fig. 8], there are two low-transmission spectral ranges 127.2-134.5GHz and 138.6-148.0GHz with center frequencies of 130.8GHz and 143.3GHz (gray regions in Fig. 8(c)). Within these regions, the transmission is lower than -6.34 dB compared to -2dB outside of these regions. The boundaries of the regions are defined as having e^{-1} value

Optics EXPRESS

by field (-4.34 dB) relative to that outside of these regions (-2dB). It is remarkable that the spectral positions of these low transmission windows correspond almost exactly to the position of the theoretically predicted bandgaps for the fundamental HE_{11}-like mode (gray regions in Fig. 5(a)), thus confirming an excellent agreement between the theoretical predictions and experimental measurements. At the same time, we observe that we were not successful in the excitation of the HE_{21} mode which we planned to use for dispersion compensation. There are several possible reasons for this. First, although, WBG1 was designed to operate with the HE_{21} mode within the bandgap of the HE_{11}-like mode, its theoretical excitation efficiency is low ($|C_{HE21}|^2$<5%, see Fig. 5(a)). Furthermore, low excitation efficiency of the HE_{21} mode can be related to its higher (than HE_{11}-mode) absorption and scattering losses, as well as higher sensitivities to the alignment errors.

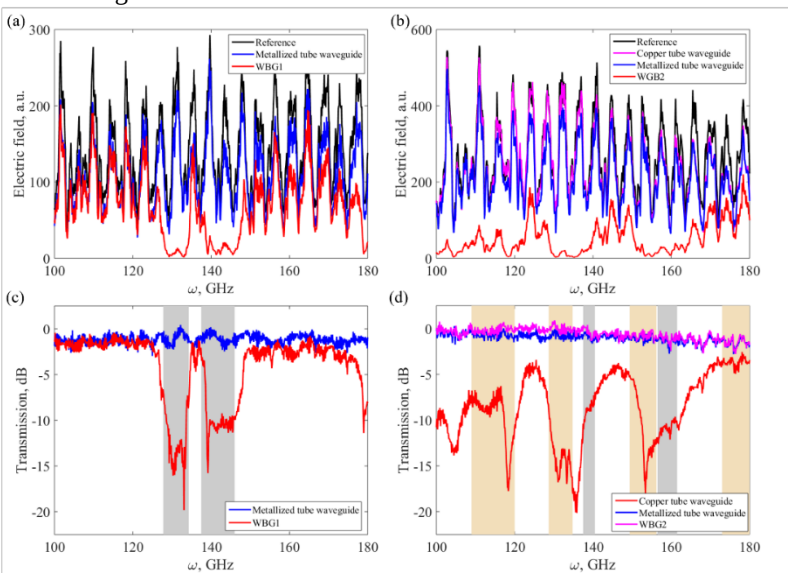

Fig. 8 (a) and (b) Measured electric fields. (c) and (d) Corresponding transmission spectra of the fabricated WBGs, polished copper tubes and uniform metalized plastic tubes. Left column: WBG1. Right column: WBG2. Gray regions in (c) and (d) corresponds to the spectral ranges where WBGs are effectively single mode. Beige regions refer to the bandgaps of the fundamental HE_{11} mode.

We now consider the WBG2. First, we observe the four low transmission windows (beige bands in Fig. 8(d)) with center frequencies of 118GHz, 135GHz, 153GHz, and 187GHz that have transmission losses over 15dB. These regions coincide well with the theoretically predicted regions of week excitation of the HE_{11}-like mode shown as beige bands in Fig. 4(b). These spectral regions correspond either to the bandgaps for the HE_{11}-like mode or the regions of anticrossing with the higher order or plasmonic modes. Outside of these low transmission regions, and near the target operational frequencies of 140GHz and 160GHz the transmission amplitude is in the -10dB to -5dB range, as seen from Fig. 8(d).

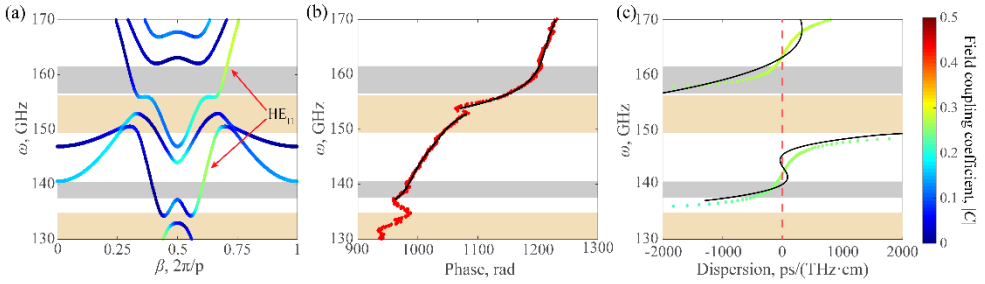

Optics EXPRESS

Fig. 9 (a) Numerically computed band diagram of the WBG2. (b) The measured phase (red dots), a corresponding polynomial fitting (black solid lines). (c) The comparison between the experimentally measured dispersion (black solid lines) and the theoretically computed dispersion of the fundamental HE_{11}-like mode (colored dots).

Finally, in Fig. 9, we present comparison of the experimentally measured and theoretically predicted group velocity dispersions for the second waveguide Bragg grating. Experimentally measured GVD is computed from the phase data as $\partial^2(\varphi/L)/\partial\omega^2$, where φ is the measured phase and L is the waveguide length. Before computing second order derivative, a fifth order polynomial fitting is used on the experimental data in order to alleviate the noise contribution (see Fig. 9 (b)). Theoretical dispersion is computed using the dispersion relation of the mode with the highest coupling coefficient to the excitation Gaussian beam shown in Fig. 9(a). In the single mode regions (shown in gray in Fig. 9), both theoretical and experimental results confirm the strong negative dispersions of the WBG2 dispersion compensator. Thus, in the 137-141GHz range, the experimentally measured dispersion varies from -500 to -100 ps/(THz · cm), while in the 156-162GHz range, dispersion varies from -2000 to -60 ps/(THz · cm). The numerical results show good match with the experimentally measure ones.

5.2 Model imaging of the waveguide output

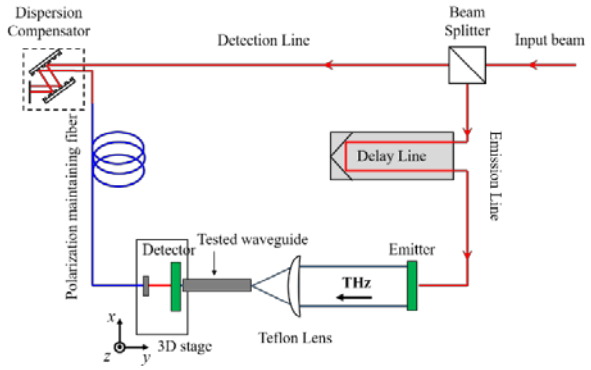

Fig. 10 Schematic of the setup used for near field imaging.

Next, we investigate the single mode operation of our waveguide Bragg gratings by mapping the model distribution of the electric field ($|\boldsymbol{E_y}|$) at the waveguide output end as a function of frequency. Model images of the output field profiles were obtained using a terahertz time-domain spectroscopy (THz-TDS) fiber-coupled imaging system. The schematic of this imaging system is shown in Fig. 10. There, the emitter, comprising of an interdigitated antenna array (*Batop*®) and a silicon lens, is used for generating a slightly divergent THz beam which is then focused onto the waveguide using a Teflon lens. The detector antenna is placed behind a metallic pinhole of 1mm diameter, mounted on a 3D stage, and it is optically excited using a polarization maintaining fiber/lens combination. The gap between the pinhole and the waveguide output facet is about 0.5mm, which is much smaller than the wavelength at 140GHz (~2mm). With a scaning range of 9×9mm and a step size of 0.25mm, the scanning provides a modal pattern with 37×37 pixels at each frequency.

Optics EXPRESS

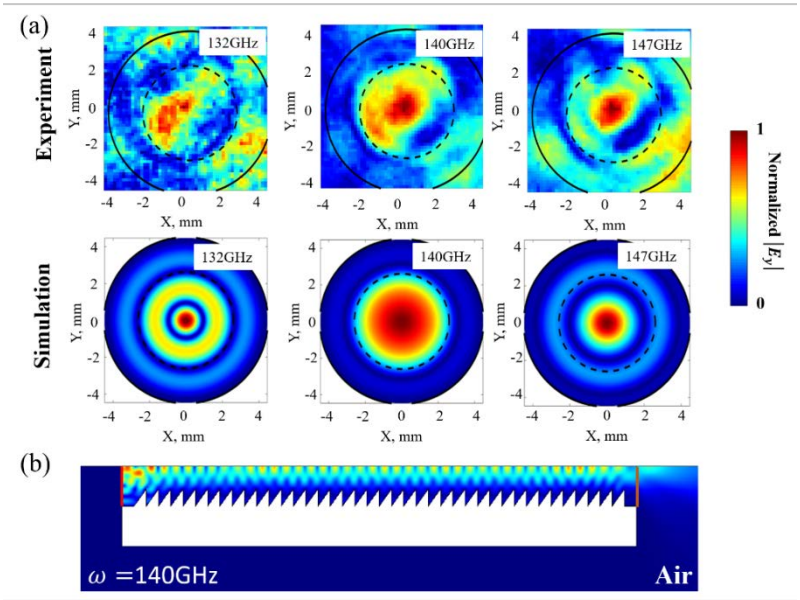

Fig. 11 (a) Modal images (upper row) and corresponding simulations (lower row) of the normalized output $|\boldsymbol{E_y}|$ field profile of the WBG2 for frequencies in the vicinity of 140GHz. The black solid circle refers to the waveguide core edge, while the dashed circle shows the boundary of central areas without the presence of periodic structures. (b) Electric field amplitude distribution at 140GHz along the cross-section of the entire WBG2 waveguide. Red solid line: input end. Orange solid line: output end.

In Fig. 11(a) we present results obtained for the WBG2 in the vicinity of 140GHz, where according to the numerical calculations (see Fig. 6) only the fundamental HE_{11}-like mode is excited by the external Gaussian beam. Hence, we expect a Gaussian-like modal distribution at the waveguide output at these frequencies. In the top row of Fig. 11(a), we present normalized electric field profiles $(|\boldsymbol{E_y}|)$ at selected frequencies as measured experimentally. For comparison, in the bottom row of Fig. 11(a), we present electric field profiles at the same frequencies as used in the experiments computed by using the finite element software COMSOL. The computation cell was that of the cross-section of the entire WBG2 waveguide in the plane containing the waveguide axis of rotational symmetry. Rotational symmetry was used and only the angular momentum $m = 1$ was retained. The computational cell was terminated in the transverse direction by the perfect electric conducting boundary to simulate the metal-air interface. At the input end (see red solid line in Fig. 11(b)), the source in the form of a Gaussian beam with a beam waist of 2λ was used (see Eq. (6)). The theoretical electric profiles were reconstructed from the computed modal distribution at the output end (see beige solid line in Fig. 11(b)). For clarity of demonstration, we highlight the central area without the presence of periodic corrugation using dashed circles, while indicating the position of the metallic boundary with a solid black line. We note that the measured field distribution is not symmetric. This may be caused by the misalignment of the waveguide input end and off-center coupling of the THz beam to guided modes of WBG2 in the experiment. The modal images show good agreements with the theoretical predictions. Thus, at 140GHz, both the experimental and theoretical images show Gaussian-like electric profiles in the central core region (region without corrugation), which confirms the single mode operation at this frequency. Meanwhile, outside of the single mode operation range (132GHz and 147GHz), the images show hybridization of the fundamental HE_{11}-like mode with the higher order modes, thus resulting in the field distributions with non-Gaussian-like profiles.

6. Discussion

Optics EXPRESS

In this paper, we proposed two waveguide Bragg gratings for the dispersion compensation in the THz frequency range. Both of these WBGs support single mode operation in the vicinity of 140GHz, where the dispersion of the dominant mode, namely the HE_{12} mode for the WBG1 and the fundamental HE_{11}-like mode for the WBG2, can be large and negative. In what follows we provide several examples of the dispersion compensation at 140GHz using the waveguide Bragg gratings proposed in our paper. For simplicity, we use $D_{WBG} \sim -250\ ps/(THz \cdot cm)$ as a typical dispersion of our WBGs.

We start with a short-range THz wireless communication link of $L_{air} = 250m$. At 140GHz, the dispersion of dry gas is $D_{air} = 2.5\times10^{-4} ps/(THz \cdot cm)$. Thus, to compensate for the dispersion in a short-range wireless link, the length of the used WBG must be $L_{WBG} = -D_{air} \cdot L_{air}/D_{WBG} \sim 1mm$. This is a very short device length, which is probably impractical since it is comparable to a single period used in our gratings. At the same time, we note that because dispersion in dry air is very small, dispersion compensation in a short-range communication link will only be necessary for extremely high bit rates. For example, for a link length of $L_{air} = 250m$, dispersion compensation should be applied at rates higher than $1/(4\sqrt{D_{air} \cdot L_{air}}) \sim 100Gbit/s$, which are currently largely unattainable.

On the other hand, for much longer THz wireless links, such as backup links for satellite assisted communications [41], transmission lengths can be hundreds of kilometers long. For them, devices with high values of GVD will be essential. For example, consider a satellite link of $L_{air} = 100km$. In this case, dispersion compensation should be applied for bit rates higher than 5Gbit/s, which makes dispersion compensation unavoidable. The corresponding WBG device length will then be $L_{WBG} \sim 10$cm, which is the device size used in this paper.

Moreover, one can envision that THz fiber-based links can be used as backup links for wireless THz communications in complex environments. As most THz fibers feature relatively high dispersions of $D_f \sim 10\ ps/(THz \cdot cm)$, use of dispersion compensation is practically unavoidable. For instance, for a THz fiber-based backup link of $L_f = 2m$, the bitrate without dispersion compensation will be limited to 8Gbit/s. To increase the link bitrate, one could use dispersion compensation with a WBG of length $L_{WBG} = -D_f \cdot L_f/D_{WBG} \sim 8cm$, which is again close to the device length used in this paper.

7. Conclusion

Two hollow core waveguide Bragg gratings operating in the transmission mode and featuring periodically arranged triangular axisymmetric slopes on their inner surface are proposed for the dispersion compensation in the terahertz frequency range. The waveguides are designed and optimized for the dispersion compensation in the vicinity of 140GHz and exhibit single mode operation, large negative dispersions $\sim -100's\ ps/(THz \cdot cm)$, and good coupling to the external Gaussian THz beam of the $\sim 2\lambda$ waist size. Using the numerically optimized waveguide structures, we then fabricated the corresponding waveguide Bragg gratings using a 3D stereolithography system, and subsequently metalized it using silver wet chemistry. Optical properties of the fabricated waveguide Bragg grating were then characterized experimentally using terahertz continuous wave spectroscopy, as well as modal imaging at the waveguide output end. Experimental findings reproduced well the theoretically predicted modal properties, including spectral positions of the high and low transmission regions as well as values of the modal dispersion within these regions. From this, we conclude that presented devices show single mode operation, relatively high coupling efficiency, and strong negative dispersions, which make the proposed devices suitable for dispersion compensation in the free-space and fiber links for the upcoming terahertz communications applications.